INTERNATIONAL JOURNAL FOR NUMERICAL METHODS IN FLUIDS
Int. J. Numer. Meth. Fluids 2000; **34**: 495–525

A nonconforming spectral element ocean model

Julia G. Levin*[,1], Mohamed Iskandarani and Dale B. Haidvogel

Institute of Marine and Coastal Sciences, Rutgers University, New Brunswick, NJ, U.S.A.

SUMMARY

A nonconforming spectral element ocean model, which allows a combination of higher- and lower-order elements in a single formulation, is presented. The choice between the order of interpolating polynomials and the number of elements can be adjusted locally in a subregion of a domain, based on the geometric and dynamic properties of a solution. High-order elements are applied in regions with smooth properties and achieve high-order convergence rates. In the regions where smoothness of the solution is limited and/or geometric requirements are complex, low-order elements are used. This paper presents a nonconforming spectral element method based on mortar elements. Convergence of the method is analyzed using several elliptic and hyperbolic test problems in two and three dimensions. To test the method, a study of wave propagation through a nonconforming interface for two problems in a realistic geometry is also presented. Copyright © 2000 John Wiley & Sons, Ltd.

KEY WORDS: mortar elements; nonconforming methods; ocean modeling

1. INTRODUCTION

Spectral element methods are relative newcomers to geophysical modeling. The potential of spectral element methods in atmospheric and oceanic modeling has been demonstrated in References [1–7]. Their three main attractive properties are rapid convergence rates due to the spectral interpolation within each element, geometrical flexibility due to the local and unstructured nature of their grids, and good scalability characteristics on parallel computers due to dense computational kernels and sparse communication requirements.

One of the main features of the spectral element method is that the order of the interpolation polynomial, N, and the number of elements, K, can be adjusted to suit the problem at hand. The optimal pair (N, K) is often a compromise among computational cost, geometrical complexity and convergence rate. If the solution is infinitely smooth and the geometry is simple, a high N and a low K yields the most efficient solution for a given error

* Correspondence to: Institute of Marine and Coastal Sciences, Rutgers University, 71 Dudley Road, New Brunswick, NJ 08901, U.S.A. Tel.: +1 732 9326555, ext. 264; fax: +1 732 9328578.
[1] E-mail: julia@imcs.rutgers.edu

Received 20 November 1998
Revised 24 January 2000

tolerance. On the other hand, a low N and a high K is more appropriate if the smoothness of the solution is limited or if the geometrical requirements are complex.

To date, geophysical spectral element models have relied on the classical conforming formulation of the spectral element method that imposes the C^0 continuity of the solution across element boundaries. This continuity is maintained by restricting the polynomial order to be fixed throughout the domain and by allowing elements to intersect along entire edges or at corners only. These two restrictions prohibit the optimization of the spectral element method over the entire domain when different flow regimes and/or geometrical requirements are present within a single simulation. In the context of ocean modeling, this situation arises, for example, when simulating cross-shelf exchanges: the spatial scale off-shore is the Rossby radius of deformation, which is roughly 40 km at mid-latitude, while the on-shore scales are smaller, of the order of hundreds of meters to a few kilometers, and are usually set by narrow topographic or coastline features.

In the present article, we present a nonconforming spectral element method designed to bypass the geometric restrictions imposed by the conforming formulation. This nonconforming formulation allows elements to intersect along a part of an entire edge and to have different spectral expansions. Such elements provide additional flexibility of h- and p-type refinement depending on the properties of the solution, domain regularity and other considerations. The regions with smooth properties can then achieve the rapid convergence of high-order schemes, while the regions of abrupt change (irregular coastline, fronts, sharp topographic features, etc.) can be resolved with finite element or low-order spectral element schemes, whose convergence is less dependent on the solution or domain regularity and whose stability requirements are less stringent than those for high-order schemes. In this paper we do not address the applications of the algorithm to adaptive grids. We concentrate on problems where the nature of the flow is known *a priori*, like resolving coastal dynamics or looking at circulation in the vicinity of ocean ridges, etc.

The differences in formulation between conforming and nonconforming problems is in a lack of C^0 continuity on the nonconforming edges, i.e., the edges where the nodes of neighboring elements do not coincide. Instead, a patching mechanism is introduced on those edges. There are several approaches to implement the patching. One solves the problem using an iterative patching technique, where each iteration involves solving problems on subdomains and then checking an agreement between the solutions on the interface. Depending on the type of matching conditions, the subproblems have either Dirichlet or mixed Dirichlet–Neumann boundary conditions on the interface. Different matching conditions for the interface have been suggested in the literature; a C^1 condition on the interface is introduced in Reference [8] for the collocation method. In Reference [9], different integral matching conditions are analyzed for Galerkin spectral and finite element methods.

The nonconforming matching in our models is performed by a mortar element method, which has been proposed by Maday *et al.* [10] and developed in References [11–13]. In the mortar method, the patching is done through an auxiliary interface called a mortar. The solution on the mortar is obtained by solving a minimization problem on the interface, and the values on the nonconforming element edges are obtained by projecting the mortar solutions back to the edges. The spaces used in the formulation of the interface problem and in the projection operators may vary. Convergence properties of several matching conditions for

spectral and finite element mortar problems are analyzed in Reference [13], where it is proven that spectral convergence can be achieved with the proper choice of matching conditions.

The choice of the mortar element method is motivated by the elegance of the formulation, the good convergence properties of the scheme and the relative ease of obtaining the nonconforming formulation from a conforming formulation (our nonconforming model is built upon the parallel spectral element ocean model (SEOM) of Iskandarani *et al.* [3]; Iskandarani M, Haidvogel DB, Levin JG. A three-dimensional spectral element ocean model. *JCP* (submitted)].

In the references above, the mortar element method is constructed for two-dimensional problems. It can be easily generalized to three dimensions if the grid is conforming in the vertical. In ocean modeling, the vertical structure of the grid is usually much simpler than the horizontal structure. In fact, most of the existing ocean models employ structured grids in the vertical. (For a recent review, see Haidvogel and Beckmann [14].) For such models, a nonconforming formulation in the vertical is not needed. Accordingly, we present here a three-dimensional SEOM with nonconforming formulation in the horizontal and conforming in the vertical.

The paper is organized as follows. A brief description of the three-dimensional SEOM is given in Section 2. Section 3 describes the two-dimensional mortar element formulation. This is followed by Section 4, where the mortar formulation is extended to three dimensions. Section 5 analyzes the performance of the model on several test problems amenable to analytical solutions in two and three dimensions. It is shown that nonconforming simulations have convergence rates that are similar to the conforming ones, a result that agrees with the analytic convergence results of Bernardi *et al.* [13]. Section 6 gives the results of two simulations in the Northwest Atlantic as an example of a realistic application of the model.

2. SPECTRAL ELEMENT OCEAN MODEL

2.1. Equations

The equations governing the basin-scale oceanic flows are the hydrostatic Boussinesq primitive equations

$$\frac{\mathrm{D}\mathbf{u}}{\mathrm{D}t} + \mathbf{f} \times \mathbf{u} + g\nabla\zeta + \nabla p = \nabla\cdot(\alpha\nabla\mathbf{u}) + \frac{\partial}{\partial z}\left(\nu\frac{\partial \mathbf{u}}{\partial z}\right)$$

$$\frac{\partial p}{\partial z} = -g\frac{\rho}{\rho_0}$$

$$\nabla\cdot\mathbf{u} + \frac{\partial w}{\partial z} = 0 \tag{1}$$

supplemented with conservation equations for temperature and salt concentration, and an equation of state linking density to temperature and salinity

$$\frac{\mathrm{D}}{\mathrm{D}t}\begin{pmatrix}T\\S\end{pmatrix}=\nabla\cdot\left[\alpha_t\nabla\begin{pmatrix}T\\S\end{pmatrix}\right]+\frac{\partial}{\partial z}\left[v_t\frac{\partial}{\partial z}\begin{pmatrix}T\\S\end{pmatrix}\right] \tag{2}$$

$$\rho=\rho(T,S)$$

Here, $\mathbf{u}$ is the horizontal velocity vector, w is the vertical velocity, $\mathbf{f}$ is the vertical Coriolis vector, g is the gravitational acceleration, ζ is the surface displacement, ρ_0 is a constant reference density, $\rho(\mathbf{x}, z, t)$ is the departure of the total density from ρ_0, and p is the baroclinic pressure scaled by ρ_0. Further, α and v are the horizontal and vertical viscosity coefficients; α_t and v_t are the horizontal and vertical diffusion coefficients; and T and S are the fields of temperature and salinity respectively. Finally, ∇ stands for the two-dimensional horizontal gradient operator and $\mathrm{D}/\mathrm{D}t$ is the material derivative following a fluid particle:

$$\frac{\mathrm{D}(\ \ )}{\mathrm{D}t}=\frac{\partial(\ \ )}{\partial t}=\mathbf{u}\cdot\nabla(\ \ )+w\frac{\partial(\ \ )}{\partial z} \tag{3}$$

The velocity boundary conditions at the top and bottom surfaces are the kinematic boundary conditions of no-normal flow

$$\frac{\partial\zeta}{\partial t}+\mathbf{u}\cdot\nabla\zeta=w \quad \text{on } z=\zeta \tag{4}$$

$$\mathbf{u}\cdot\nabla h=-w \quad \text{on } z=-h \tag{5}$$

and the dynamic boundary conditions specifying the stresses

$$\left(\alpha\nabla\mathbf{u}+v\frac{\partial\mathbf{u}}{\partial z}\mathbf{k}\right)\cdot\mathbf{n}=\boldsymbol{\tau} \quad \text{on } z=\zeta \tag{6}$$

$$\left(\alpha\nabla\mathbf{u}+v\frac{\partial\mathbf{u}}{\partial z}\mathbf{k}\right)\cdot\mathbf{n}=-\gamma\mathbf{u} \quad \text{on } z=-h \tag{7}$$

where $\boldsymbol{\tau}$ is the prescribed wind stress, $\mathbf{n}$ is the outward unit normal, $h(\mathbf{x})$ is the resting depth, and γ is the drag coefficient.

On the lateral boundaries, we apply either a no-slip boundary condition

$$\mathbf{u}=0 \tag{8}$$

or free-stress boundary conditions

$$\mathbf{u}\cdot\mathbf{n}=\nabla(\mathbf{u}\cdot\mathbf{t})\cdot\mathbf{n}=0 \tag{9}$$

where $\mathbf{t}$ is the tangent to the boundary in the horizontal direction. Notice that no boundary conditions are needed for w on the lateral surfaces of the domain, as w is computed diagnostically from the continuity equation.

The boundary conditions for the tracers are of the Neumann type

$$\left(\alpha_t \nabla T + v_t \frac{\partial T}{\partial z}\mathbf{k}\right)\cdot\mathbf{n} = Q \tag{10}$$

$$\left(\alpha_t \nabla S + v_t \frac{\partial S}{\partial z}\mathbf{k}\right)\cdot\mathbf{n} = B \tag{11}$$

where Q and B are the specified fluxes of heat and salinity respectively.

The presence of the free surface gives rise to surface gravity waves that travel at speeds much larger than those of other phenomena of interest. The common strategy, which we follow here, is to isolate the gravity waves in a set of two-dimensional equations, which are integrated separately from the three-dimensional equations. The two-dimensional equations are similar to the shallow water equations and can be obtained by vertical integration of the three-dimensional momentum and continuity equations

$$\frac{\partial \zeta}{\partial t} + \nabla\cdot[(h+\zeta)\mathbf{U}] = 0$$

$$\frac{\partial \mathbf{U}}{\partial t} + \mathbf{U}\cdot\nabla\mathbf{U} + \mathbf{f}\times\mathbf{U} + g\nabla\zeta = \frac{\boldsymbol{\tau}}{\rho_0(h+\zeta)} - \frac{\gamma\mathbf{u}|_{-h}}{h+\zeta} + \mathbf{D} - \mathbf{C} \tag{12}$$

where $\mathbf{U}$ is the depth-average velocity

$$\mathbf{U} = \frac{1}{h+\zeta}\int_{-h}^{\zeta} \mathbf{u}\ \mathrm{d}z \tag{13}$$

$\mathbf{D}$ represents the effect of the horizontal viscous dissipation on the depth-mean flow, and $\mathbf{C}$ is the coupling term between the two- and three-dimensional momentum equations.

2.2. Mapping of the free surface

Because the surface is moving, the domain V occupied by the fluid is time-dependent. In order to simplify the calculations, we map our domain to a steady computational space $(\mathbf{x}, Z, t)$, where

$$Z(\mathbf{x}, z, t) = h\frac{z-\zeta}{h+\zeta} \tag{14}$$

The height $z\in[-h, \zeta]$ is thus mapped into the interval $Z\in[-h, 0]$.

Under this transformation, the horizontal gradient, material derivative and divergence operators become

$$\nabla\Phi = \nabla_Z\Phi - \frac{\partial\Phi}{\partial Z}\frac{\partial Z}{\partial z}\nabla_Z z \tag{15}$$

$$\frac{\mathrm{D}\Phi}{\mathrm{D}t} = \left.\frac{\partial\Phi}{\partial t}\right|_Z + u\left.\frac{\partial\Phi}{\partial x}\right|_Z + v\left.\frac{\partial\Phi}{\partial y}\right|_Z + W\frac{\partial\Phi}{\partial Z} \tag{16}$$

$$\nabla\mathbf{u} + \frac{\partial w}{\partial z} = \nabla_Z\cdot\mathbf{u} + \frac{\partial W}{\partial Z} + \frac{\partial Z}{\partial z}\frac{\mathrm{D}}{\mathrm{D}t}\left(\frac{\partial z}{\partial Z}\right) \tag{17}$$

where $\partial/\partial x|_Z$, $\partial/\partial y|_Z$ and ∇_Z denote the x and y derivatives and the horizontal gradient operator along constant Z-lines respectively. W is the vertical velocity in the mapped space

$$W = \frac{\mathrm{D}Z}{\mathrm{D}t} = \frac{\partial Z}{\partial z}\left(w - u\left.\frac{\partial z}{\partial x}\right|_Z - v\left.\frac{\partial z}{\partial y}\right|_Z - \left.\frac{\partial z}{\partial t}\right|_Z\right) \tag{18}$$

The Jacobian of the mapping between the unsteady physical domain and the steady computational domain is

$$J_s = \frac{\partial Z}{\partial z} = 1 + \frac{\zeta}{h} \approx 1 + O\left(\frac{\zeta}{h}\right) \tag{19}$$

which is approximately equal to 1, as $\zeta \ll h$, except for the inner continental shelves and estuaries. This approximation amounts to neglecting variations in the volume of fluid owing to the surface displacement. It results in a tremendous saving in computational effort, as the three-dimensional mass matrix becomes steady in time and need not be updated. This mapping has the additional benefit of preserving the structure of the three-dimensional equations, provided the advection terms are evaluated with the new vertical velocity W.

2.3. Variational formulation

The variational formulation of equation (1) is

$$\begin{aligned}&\int_V \Phi\left[\frac{\mathrm{D}\mathbf{u}}{\mathrm{D}t} + \mathbf{f}\times\mathbf{u} + g\Delta\zeta + \nabla p\right]\mathrm{d}V \\ &= -\int_V\left[\alpha\nabla\mathbf{u}\cdot\nabla\Phi + \nu\frac{\partial\mathbf{u}}{\partial z}\frac{\partial\Phi}{\partial z}\right]\mathrm{d}V + \int_{\partial V_\mathrm{f}}\boldsymbol{\tau}\Phi\,\mathrm{d}S - \int_{\partial V_\mathrm{b}}\gamma\|\mathbf{u}\|\mathbf{u}\Phi\,\mathrm{d}S\end{aligned} \tag{20}$$

where Φ is the three-dimensional test function associated with the velocity and tracer fields. ∂V_f refers to the free surface boundary and ∂V_b refers to the seabed boundary. The boundary integrals weakly enforce the Neumann and Robin (mixed) boundary conditions imposed on the velocity field. Essential boundary conditions are enforced by zeroing the test function Φ on those portions of the boundary where the boundary conditions are of Dirichlet type, and setting $\mathbf{u}$ equal to the imposed boundary value, e.g., zero on no-slip walls.

Likewise, the variational formulation of Equation (2) is given by

$$\int_V \Phi \frac{\mathrm{D}}{\mathrm{D}t}\begin{pmatrix} T \\ S \end{pmatrix} \mathrm{d}V = -\int_V \left[\alpha_t \nabla \begin{pmatrix} T \\ S \end{pmatrix} \cdot \nabla \Phi + \nu_t \frac{\partial}{\partial z}\begin{pmatrix} T \\ S \end{pmatrix} \frac{\partial \Phi}{\partial z} \right] \mathrm{d}V + \int_{\partial V_\Gamma} \begin{pmatrix} Q \\ B \end{pmatrix} \Phi \, \mathrm{d}S \tag{21}$$

The continuity equation is differentiated in the vertical before integration in order to ease the imposition of surface and bottom boundary conditions. Its variational formulation becomes

$$\int_V \frac{\partial \Phi}{\partial z}\frac{\partial W}{\partial z}\,\mathrm{d}V = \int_V \frac{\partial \Phi}{\partial z}\frac{\partial Z}{\partial z}\left(\mathbf{U}\cdot\frac{\nabla h}{h} - \frac{\partial Z}{\partial z}\nabla_Z \cdot \left[\frac{\partial z}{\partial Z}(\mathbf{u}-\mathbf{U}) \right] \right) \mathrm{d}V \tag{22}$$

The variational formulation of the barotropic equations is

$$\begin{aligned} &\int_A \Psi^{N-2}\frac{\partial \zeta}{\partial t}\,\mathrm{d}A - \int_A (h+\zeta)\mathbf{U}\cdot\nabla\Psi^{N-2}\,\mathrm{d}A = \int_{\partial A} \Psi^{N-2} q \,\mathrm{d}l \\ &\int_A \Psi^N \left[\frac{\partial \mathbf{U}}{\partial t} + \mathbf{U}\cdot\nabla\mathbf{U} + \mathbf{f}\times\mathbf{U} + g\nabla\zeta \right] \mathrm{d}A \\ &= \int_A \Psi^N \left[\frac{\boldsymbol{\tau}}{\rho_0(h+\zeta)} - \frac{\gamma \mathbf{u}|_{-h}}{h+\zeta} \right] \mathrm{d}A + \int_A \Psi^N [\mathbf{D}-\mathbf{C}]\,\mathrm{d}A \end{aligned} \tag{23}$$

where Ψ^{N-2} and Ψ^N refer to the two-dimensional test functions associated with ζ and $\mathbf{U}$ respectively. The divergence term in the continuity equation has been integrated by parts to allow the imposition of the inflow as weak boundary conditions. The q in Equation (23) refers to the inflow per unit width. Notice that the integrals in the above equations are performed over a horizontal surface.

In each element all the variables are expanded in a series of Legendre cardinal functions of the form

$$\mathbf{u}(\xi,\eta,\sigma) = \sum_{i,j=0}^{N}\sum_{k=0}^{N^\sigma} u_{ijk} h_i^N(\xi) h_j^N(\eta) h_k^{N^\sigma}(\sigma) \tag{24}$$

for a three-dimensional variable, and

$$\begin{aligned} \mathbf{U}(\xi,\eta) &= \sum_{i,j=0}^{N} \mathbf{U}_{ij} h_i^N(\xi) h_j^N(\eta) \\ \zeta(\xi,\eta) &= \sum_{i,j=0}^{N-2} \zeta_{ij} h_i^{N-2}(\xi) h_j^{N-2}(\eta) \end{aligned} \tag{25}$$

for two-dimensional variables, where h_i^N is a Legendre cardinal function of order N. The ζ collocation points are staggered with respect to those of $\mathbf{U}$ in order to eliminate spurious pressure oscillations when the barotropic flow is almost divergence-free [3]. Notice that we have kept the order of the interpolation in the vertical and horizontal directions separate, as the vertical and horizontal structures of the solution may be quite different. It is best to keep

the orders of the vertical and horizontal interpolations independent so that they can be adjusted individually to achieve the best h–p balance in each direction.

The interpolations (24) and (25) are substituted into the Galerkin formulation to yield a system of ordinary differential equations, after setting

$$\Phi = h_i^N(\xi)h_j^N(\eta)h_k^{N^\sigma}(\sigma)$$

$$\Psi^N = h_i^N(\xi)h_j^N(\eta)$$

$$\Psi^{N-2} = h_i^{N-2}(\xi)h_j^{N-2}(\eta)$$

and evaluating the resulting integrals numerically.

The conforming formulation is based on the C^0 continuity of the functions of the form of Equations (24) and (25) across the edges of the elements. For more details on the formulation, the reader is referred to Reference [3]; Iskandarani *et al.* (submitted)]. Sample applications are described in References [1,2,4,7].

3. TWO-DIMENSIONAL MORTAL ELEMENT FORMULATION

Our mortar element formulation is based on the approach presented in References [10,11,13]. In the formulation of References [10,11], spectral expansions are the same in all elements and a nonconforming grid is obtained by h-refinement and mesh sliding. In Reference [13], coupling of spectral and finite element methods is analyzed. Our method is designed for geometrically nonconforming grids where elements are allowed to have different spectral expansions. The method is easily extendable to include coupling to finite element grids. The method uses a different algorithm for constructing a mortar interface than the ones suggested in References [10,11,13]. As a result, a different formulation of a projection operator between interface and nonconforming element edges is obtained. Section 3.1 describes an algorithm for constructing a mortar skeleton that connects the nonconforming element edges. It then formulates discrete spaces for the mortars and the edges, and defines an appropriate projection operator between them. Section 3.2 specifies a set of basis functions for all the spaces in the formulation. The basis functions are then used in Section 3.3 to obtain a linear projection operator between a mortar interface and its neighboring edges. In Section 3.4, the projection operators of Section 3.3 and the spectral element formulation of Section 2 are combined in a minimization problem for the interface.

3.1. Formulation of discrete spaces

Our nonconforming formulation consists of a set of conforming spaces for those regions that permit a conforming formulation, a space of functions on a mortar interface (mortar space), and a space used in a projection between the mortar space and the conforming spaces.

Consider a two-dimensional region Ω. Let Ω consist of several subregions Ω_p, $p = 1, \ldots, P$, such that in each of Ω_p the spectral element grid is conforming, and such that the subregions

cover Ω completely: $\cup \Omega_p = \Omega$, and intersect with each other only along a collection of one-dimensional element edges. We denote the union of these elemental edges by S, and the collection of conforming spectral elements in each of Ω_p by Ω_p^k, $k = 1, \ldots, K^p$.

The nonconforming formulation starts by defining a standard conforming discrete space X^p [15,16] in each subdomain Ω_p

$$X^p(\Omega_p) = \{v \in C^0(\Omega_p):\ \forall k = 1, \ldots, K^p,\ v|_{\Omega_p^k} \in P_{N_p} \times P_{N_p}(\Omega_p^k),\ v|_{\partial\Omega} = 0\} \tag{26}$$

where N_p is the spectral expansion used in each element Ω_p^k of a subregion Ω_p, $P_{N_p}(\Omega_p^k)$ is the space of polynomials of order not greater than N_p, and $\partial\Omega$ is the boundary of the domain Ω.

The conforming formulation (26) is valid everywhere except on those element edges that belong to S. On S, the nodal points that come from the neighboring elements do not coincide, and thus it is impossible to come up with a single spectral expansion that is consistent with the spectral expansions in the two neighboring elements simultaneously. To control the error between the two representations of the solution on S, the mortar element approach introduces as auxiliary space W, which works as a link between the two different representations.

The space W depends on the way the skeleton S is split into segments. Let us split S into a collection of line segments γ_i, $i = 1, \ldots, \bar{M}$, such that end points of each segment γ_i coincide with a vertex in all the subdomains Ω_p, which share this portion of S (Figure 1). Line segment γ_i is called a mortar. Then, the mortar space W can be defined as follows:

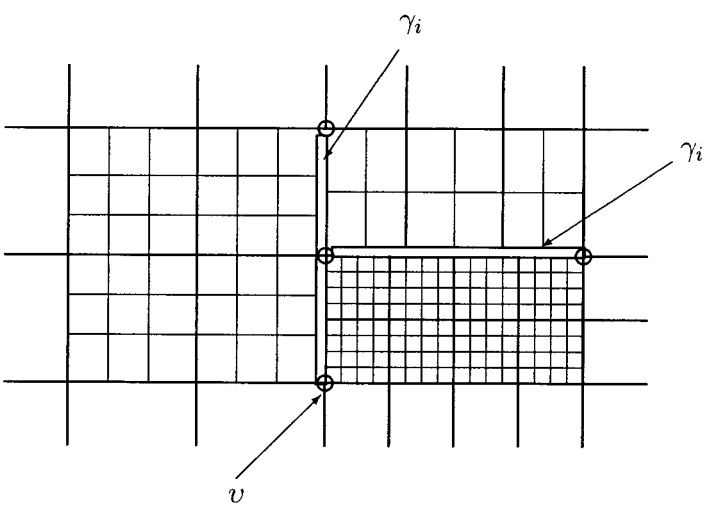

Figure 1. Example of a nonconforming grid. Element edges are shown with thicker lines, grid lines are shown with thinner lines. Mortar endpoints are denoted by circles. Mortars are denoted by two thick lines. Here, collocation nodes are shown equally spaced, while in reality they are denser near element edges.

$$W = \{\phi \in C^0(S):\ \forall i = 1, \ldots, \bar{M},\ \phi|_{\gamma_i} \in P_{\bar{N}_i}(\gamma_i),\ \phi|_{\partial\Omega} = 0\} \tag{27}$$

To define order $\bar{N}_i$ of polynomials $P_{\bar{N}_i}(\gamma_i)$ for each mortar γ_i we consider two sets of element edges Γ^{I}_j, $j = 1, \ldots, K^{\mathrm{I}}$ and Γ^{II}_j, $j = 1, \ldots, K^{\mathrm{II}}$, such that

- each of the sets Γ^{I}, Γ^{II} belongs to a particular subdomain from the set of Ω_p, which we denote by Ω^{I} and Ω^{II} respectively, i.e., $\forall j$, $\Gamma^{\mathrm{I}}_j \in \Omega^{\mathrm{I}}$, $\Gamma^{\mathrm{II}}_j \in \Omega^{\mathrm{II}}$,
- both sets Γ^{I}, Γ^{II} cover the mortar completely: $\cup_j \Gamma^{\mathrm{I}}_j = \gamma_i$ and $\cup_j \Gamma^{\mathrm{II}}_j = \gamma_i$, and
- end points $v^{1,2}_i$ of the mortar γ_i coincide with a vertex in both Ω^{I} and Ω^{II}.

We call Γ^{I} and Γ^{II} the two sides of the mortar γ_i.

Let N^{I} and N^{II} be spectral expansions in Ω^{I} and Ω^{II} respectively, then the order $\bar{N}_i$ of the polynomials $P_{\bar{N}_i}(\gamma_i)$ in Equation (27) is such that the number of degrees of freedom on the mortar is equal to the maximum number of degrees of freedom in the tow sets Γ^{I} and Γ^{II}

$$\bar{N}_i = \max(K^{\mathrm{I}} N^{\mathrm{I}}, K^{\mathrm{II}} N^{\mathrm{II}}) \tag{28}$$

To distinguish spectral expansions on mortars from spectral expansions on neighboring elements, parameters that are related to the mortars have an overbar.

The splitting of skeleton S into mortars is not unique. We choose a decomposition that gives the shortest possible mortars. Such a decomposition leads to a smaller dimension $\bar{N}_i$ of polynomial spaces in Equation (27), and thus to a reduced dimension of the projection operator.

There are now three different functions that can be constructed on the interface γ_i, each belonging to one of the following spaces:

$$W|_{\gamma_i} = \{v \in P_{\bar{N}_i}(\gamma_i)\}$$

$$X^p(\Omega^{\mathrm{I}})|_{\gamma_i} = \{v \in C^0(\gamma_i),\ \forall j = 1, \ldots, K^{\mathrm{I}}:\ v|_{\Gamma^{\mathrm{I}}_j} \in P_{N^{\mathrm{I}}}(\Gamma^{\mathrm{I}}_j)\}$$

$$X^p(\Omega^{\mathrm{II}})|_{\gamma_i} = \{v \in C^0(\gamma_i),\ \forall j = 1, \ldots, K^{\mathrm{II}}:\ v|_{\Gamma^{\mathrm{II}}_j} \in P_{N^{\mathrm{II}}}(\Gamma^{\mathrm{II}}_j)\} \tag{29}$$

To minimize the difference between them, we supply two additional constraints to the space $X^p(\Omega^{\mathrm{I}})|\gamma_i$ and $X^p(\Omega^{\mathrm{II}})|\gamma_i$. First, the values at the end points of γ_i should be the same in all the representations, and second, the error between the representations is orthogonal to an appropriately chosen space. We denote the resulting spaces by $X^{\mathrm{I}}(\gamma_i)$ and $X^{\mathrm{II}}(\gamma_i)$, whose definitions can be written as follows:

$$X^{\mathrm{I}}(\gamma_i) = \Bigg\{ v \in C^0(\gamma_i),\ \forall j = 1, \ldots, K^{\mathrm{I}}:\ v|_{\Gamma^{\mathrm{I}}_j} \in P_{N^{\mathrm{I}}}(\Gamma^{\mathrm{I}}_j) \text{ such that}$$
$$\exists \phi \in W:\ \phi(v^{1,2}_i) = v(v^{1,2}_i) \text{ and } \int_{\gamma_i} (v - \phi|_{\gamma_i})\psi \, \mathrm{d}s = 0\ \ \forall \psi \in \tilde{P}^{\mathrm{I}}(\gamma_i) \Bigg\}$$

$$X^{\mathrm{II}}(\gamma_i) = \Big\{ v \in C^0(\gamma_i),\ \forall j = 1, \ldots, K^{\mathrm{II}}:\ v\big|_{\Gamma_j^{\mathrm{II}}} \in P_{N^{\mathrm{II}}}(\Gamma_j^{\mathrm{II}}) \\ \text{such that } \exists \phi \in W:\ \phi(v_i^{1,2}) = v(v_i^{1,2}) \text{ and } \int_{\gamma_i} (v - \phi\big|_{\gamma_i}) \psi \, \mathrm{d}s = 0 \ \forall \psi \in \tilde{P}^{\mathrm{II}}(\gamma_i) \Big\} \quad (30)$$

where W is defined in Equation (27). The integrals in Equation (30) can be viewed as projections from a mortar space into its sides. Spaces $\tilde{P}^{\mathrm{I}}(\gamma_i)$ and $\tilde{P}^{\mathrm{II}}(\gamma_i)$ that are used in the projections are called projection spaces. They are constructed in such a way that the projections remove the small wavelengths that are resolved on the mortars but are not resolved on the adjacent element edges. Thus, definitions of $\tilde{P}^{\mathrm{I}}(\gamma_i)$ and $\tilde{P}^{\mathrm{II}}(\gamma_i)$ should be similar to definitions of $X^p(\Omega^{\mathrm{I}})\big|_{\gamma_i}$ and $X^p(\Omega^{\mathrm{II}})\big|_{\gamma_i}$ respectively, but have fewer degrees of freedom. Since there is a constraint for each of the two mortar endpoints, the projection spaces should have at least two degrees of freedom less then the number of degrees of freedom on the sides.

Then, the projection spaces can be defined as

$$\tilde{P}^{\mathrm{I}}(\gamma_i) = \{ v \in C^0(\gamma_i):\ \forall j = 1, \ldots, K^{\mathrm{I}},\ v\big|_{\Gamma_j^{\mathrm{I}}} \in P_{q_{i,j}^{\mathrm{I}}}(\Gamma_j^{\mathrm{I}}) \}$$

$$\tilde{P}^{\mathrm{II}}(\gamma_i) = \{ v \in C^0(\gamma_i):\ \forall j = 1, \ldots, K^{\mathrm{II}},\ v\big|_{\Gamma_j^{\mathrm{II}}} \in P_{q_{i,j}^{\mathrm{II}}}(\Gamma_j^{\mathrm{II}}) \} \quad (31)$$

where the orders q_{ij}^{I} and q_{ij}^{II} depend on the number of end points shared by a mortar γ_i and an element edge Γ_j^{I}, Γ_j^{II} respectively. If γ_i and Γ_j^{I} do not share an end point, then $q_{ij}^{\mathrm{I}} = N^{\mathrm{I}}$; if they share only one endpoint, then $q_{ij}^{\mathrm{I}} = N^{\mathrm{I}} - 1$; if they share both endpoints, which can happen only if a side consists of only one element edge, $\gamma_i = \Gamma_1^{\mathrm{I}}$, then $q_{ij}^{\mathrm{I}} = N^{\mathrm{I}} - 2$. Similar rules are applied to q_{ij}^{II}. The choice of the order is shown schematically in Figure 2.

Based on the definitions in Equations (27), (30) and (31), we can now specify a discrete space $X_h(\Omega)$ for the nonconforming problem

$$X_h(\Omega) = \{ v:\ \forall p = 1, \ldots, P,\ v\big|_{\Omega_p} \in X^p(\Omega_p) \text{ such that } \forall \gamma_i \in S,\ i = 1, \ldots, \bar{M}, \\ \exists \Gamma_j^{\mathrm{I}}, \Gamma_j^{\mathrm{II}}, \text{ such that } \cup_j \Gamma_j^{\mathrm{I}} = \cup_j \Gamma_j^{\mathrm{II}} = \gamma_i \text{ and} \\ v\big|_{\cup \Gamma_j^{\mathrm{I}}} \in X^{\mathrm{I}}(\gamma_i),\ v\big|_{\cup \Gamma_j^{\mathrm{II}}} \in X^{\mathrm{II}}(\gamma_i) \} \quad (32)$$

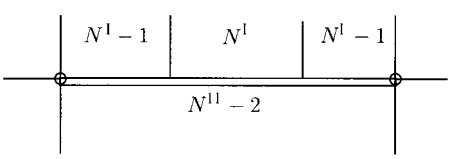

Figure 2. Order q in the definition of the projection space on the two sides of a mortar. A single mortar here contacts with three elements on one side and with one element on other side. Depending on whether the mortar and an element share a vertex, the order q is set to either $N-2$, $N-1$ or N.

Definition (32) imposes a C^0 continuity of the solution on the skeleton S through definition of the mortar space (27). Then, by definition of spaces $X^{\mathrm{I}}(\gamma_i)$ and $X^{\mathrm{II}}(\gamma_i)$ on the two sides of each mortar $\gamma_i \in S$ imposes two additional constraints, which control the error between the two different spectral representations on γ_i. First, we make the solution continuous at the mortar end points, and second, we make the error between the two spectral representations orthogonal to the space in which each side of the interface is represented.

The definitions of discrete spaces $X^{\mathrm{I}}(\gamma_i)$ and $X^{\mathrm{II}}(\gamma_i)$ that are given on the two sides of the mortar, differ from each other only in the number of elements (K^{I} versus K^{II} and the order of polynomials N^{I} or N^{II}. In the following, to simplify the notation we drop the superscripts I and II and give the definition of basis functions and projection operators for one side of the mortar only.

3.2. Definition of basis functions

According to the definition of conforming spaces $X^p(\Omega_p)$ in Section 3.1, in each element Ω_p^k of a subregion Ω_p, a function $u \in X^p(\Omega_p)$ can be interpolated with a set of Legendre cardinal functions of order N_p. Similarly, according to the definition of the mortar space in Equation (27), any function $\phi \in W$ can be interpolated in a mortar γ_i by a set of Legendre cardinal functions of order $\bar{N}_i$. Since we are going to specify basis functions for a single mortar γ_i and a basis for neighboring elements on one of the mortar sides only, in the following we drop the subscripts in both N_p and $\bar{N}_i$.

Thus, in each element Ω^k that belongs to either Ω^{I} or Ω^{II}, a variable u is interpolated as

$$u(x(\xi,\eta),\ y(\xi,\eta)) = \sum_{i,j=0}^{N} u_{ij} h_i^N(\xi) h_j^N(\eta) \tag{33}$$

where $h_i^N(\xi)$ are Legendre cardinal functions of order N

$$h_i^N(\xi) = \frac{-L'_N(\xi)(1-\xi^2)}{N(N+1)L_N(\xi_i^N)(\xi-\xi_i^N)}, \quad i=0,1,\ldots,N \tag{34}$$

$x(\xi,\eta), y(\xi,\eta)$ is a coordinate transformation from an isoparametric element into a square, $\xi, \eta \in [-1,1]$; L_N is a Legendre polynomial of order N; and ξ_i^N, $i=0,1,\ldots,N$ are Legendre–Gauss–Lobatto points of order N, i.e.,

$$\xi_i^N = \begin{cases} -1 & i=0 \\ \text{roots of } L'_N(\xi), & i=1,\ldots,N-1 \\ 1, & i=N \end{cases} \tag{35}$$

Similarly, on each element edge Γ_j, a function u can be written as

$$u(x(\xi), y(\xi)) = \sum_{n=0}^{N} u_n h_n^N(\xi) \tag{36}$$

where $x(\xi), y(\xi)$ is a transformation between an element edge Γ_j and its representation in a computation space. For more information on basis functions see References [15–17].

According to the definition of mortar space W, any function $\phi \in W$ can be interpolated in a mortar γ_i as

$$\phi(\bar{x}(\bar{\xi}), \bar{y}(\bar{\xi})) = \sum_{m=0}^{\bar{N}} \phi_m h_m^{\bar{N}}(\bar{\xi}) \tag{37}$$

where the order $\bar{N}$ of polynomial basis functions is specified according to Equation (28), and $\bar{x}(\bar{\xi}), \bar{y}(\bar{\xi})$ is a transformation between a line segment γ_i and its computational space representation $\xi \in [-1, 1]$.

A basis for projection space $\tilde{P}(\gamma_i)$ is a set of $R = KN - 1$ functions. If $\gamma_i = \Gamma_j$, then both end points of the mortar γ_i coincide with the end points of Γ_j. In this case, the basis for $\tilde{P}(\gamma_i)$ is a set of $N-1$ polynomials of order $N-2$, which have the form

$$\psi_i^{N-2}(\xi) = \frac{-L'_N(\xi)(1-\xi_i^N)(1+\xi_i^N)}{N(N+1)L_N(\xi_i^N)(\xi-\xi_i^N)}, \quad i = 1, \ldots, N-1 \tag{38}$$

where ξ_i^N, $i = 1, \ldots, N-1$ are Gauss–Lobatto points defined in Equation (35).

If $\gamma_i = \cup_{j=1}^{K} \Gamma_j$, $K > 1$, then the basis for $\tilde{P}(\gamma_i)$ consists of the union of basis functions for all the edges Γ_j. For an edge that does not share any endpoints with the mortar, the basis is a set of $N+1$ 'regular' Legendre cardinal functions of order N

$$\psi_i^N = h_i^N, \quad i = 0, 1, \ldots, N \tag{39}$$

If the edge shares one of the endpoints, then the basis function are polynomials of order $N-1$. Depending on whether the end point corresponds to $\xi_0 = -1$ or to $\xi_N = 1$, they are respectively

$$\psi_i^{N-2}(\xi) = \begin{cases} \dfrac{-L'_N(\xi)(1-\xi)(1+\xi_i^N)}{N(N+1)L_N(\xi_i^N)(\xi-\xi_i^N)}, & i = 1, \ldots, N \\ \dfrac{-L'_N(\xi)(1-\xi_i^N)(1+\xi)}{N(N+1)L_N(\xi_i^N)(\xi-\xi_i^N)}, & i = 0, 1, \ldots, N-1 \end{cases} \tag{40}$$

Function ψ_i defined in Equations (38)–(40) are constructed in such a way that they satisfy a relation $\psi_i(\xi_j) = \delta_{ij}$ for all nodal points ξ_j, except those that coincide with the end points of the mortar, where δ_{ij} is a Kronecker delta.

3.3. Projection operator

To obtain projections between a mortar γ_i and its sides, we insert interpolation formulas (36) and (37) into Equation (30) and compute the integrals

$$\int_{\gamma_i} (u-\phi)\psi_q \, \mathrm{d}S = 0$$

for each basis function of the projection space: $\psi_q \in \tilde{P}(\gamma_i)$, $q = 1, \ldots, R$ defined in Equations (38)–(40). The integral over a mortar γ_i is computed by summing up the contributions from all the element edges $\Gamma_j \subset \gamma_i$, $j = 1, \ldots, K$, while on each Γ_j, the integration is performed with Gauss–Lobatto quadratures. The order of the quadrature is N for the integration of $u\psi_q$ term and $\bar{N}$ for the integration of $\phi\psi_q$. Note that the quadrature of order N would be insufficient for an accurate integration of the terms that include ϕ, as their polynomial expansion can be of a much higher order than the quadrature order N. In a case when ψ_q is nonzero over an element edge Γ_j, the integration of the $u\psi_q$ term over Γ_j yields

$$\int_{\Gamma_j} u\psi_q \, \mathrm{d}S = \sum_{n=0}^{N} u_n \int_{-1}^{1} h_n^N(\xi)\psi_q(\xi)|s(\xi)| \, \mathrm{d}\xi = B_q u_q + R_{q0}\phi_0 + R_{q\bar{N}}\phi_{\bar{N}} \tag{41}$$

where

$$B_q = \omega_q^N |s_q^{\Gamma_j}| \tag{42}$$

$$R_{q0} = \psi_q(-1)\omega_0^N |s_0^{\Gamma_j}| \tag{43}$$

$$R_{q\bar{N}} = \psi_q(1)\omega_N^N |s_N^{\Gamma_j}|$$

ω_i^N are the weights of the quadrature of order N, and $|s_i^{\Gamma_j}|$ are metric terms, arising from the coordinate transformation between Γ_j and its representation in the computational space.

The terms R_{q0} and $R_{q\bar{N}}$ become zero if a test function ψ_q is zero at the end points $\xi = \pm 1$, which happens if ψ_q is defined in Equation (39). For those test functions that are defined in Equation (40), one of the terms in Equation (43) is nonzero; and for those that are defined in Equation (38), both terms are nonzero.

Similarly, the integration of $\phi\psi_q$ over an element edge Γ_j gives

$$\int_{\Gamma_j} \phi\psi_q \, \mathrm{d}S = \sum_{m=0}^{\bar{N}} \phi_m \int_{-1}^{1} h_m^{\bar{N}}(\bar{\xi}(\xi))\psi_q(\xi)|s(\xi)| \, \mathrm{d}\xi = \sum_{m=0}^{\bar{N}} P_{qm}\phi_m \tag{44}$$

where

$$P_{qm} = \sum_{r=0}^{\bar{N}} h_m^{\bar{N}}(\bar{\xi}(\xi_r^{\bar{N}}))\psi_q(\xi_r^{\bar{N}})\omega_r^{\bar{N}} |s_r^{\Gamma_j}| \tag{45}$$

and a function $\bar{\xi}(\xi)$ in Equations (44) and (45) is a coordinate transformation between two different representations of a same point (x, y) in the computational spaces for a mortar and for an element. It can be obtained from the relation

$$(x(\xi), y(\xi)) = (\bar{x}(\bar{\xi}), \bar{y}(\bar{\xi}))$$

where the left-hand side is a transformation between a computational space and an element edge Γ_j, and the right-hand side is a transformation between a computational space and a mortar γ_i. As the computation of $\bar{\xi}(\xi)$ involves an inverse of a coordinate transformation, which is not possible to obtain for functions of general form, we restrict ourselves to the case when a mortar lies on a straight line. In this case, the coordinate transformation becomes

$$\bar{\xi}(\xi) = \frac{2}{|\gamma_i|} s - 1 + \frac{|\Gamma_j|}{|\gamma_i|}(\xi + 1) \tag{46}$$

where $|\gamma_i|$ is the length of the mortar, $|\Gamma_j|$ is the length of the element edge, s is an offset between the mortar and the element edge (see Figure 3).

Combining Equations (41) and (44) and assembling contributions from different element edges Γ_j together, we obtain a projection operator

$$u_q = \sum_{m=1}^{\bar{N}-1} Q_{qm}\phi_m + T_{q0}\phi_0 + T_{q\bar{N}}\phi_{\bar{N}}, \quad q = 1, \ldots, R \tag{47}$$

where

$$Q_{qm} = \frac{P_{qm}}{B_q}, \qquad T_{ql} = \frac{(P_{ql} - R_{ql})}{B_q}, \quad l = 0, \bar{N} \tag{48}$$

Since each mortar connects two sides, there are in fact two projections of the form (47) for each mortar.

The projection operators (47) constructed for all mortars γ_i, $i = 1, \ldots, \bar{M}$, together with the conditions for the vertices $\phi(v_i^{1,2}) = u(v_i^{1,2})$, form a global linear projection operator

$$u^S = Q\phi \tag{49}$$

where u^S are nodal values on those element edges that require the nonconforming matching; ϕ are the nodal values on all the mortars γ_i, $i = 1, \bar{M}$. With an appropriate ordering of

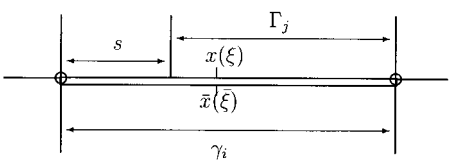

Figure 3. Relative position of an element edge Γ_j toward a mortar γ_i. Parameter s is an offset between the mortar and the edge. The same point in physical space has two different representations, one is in a coordinate system of an element, $x(\xi)$, another is in a coordinate system of a mortar, $\bar{x}(\bar{\xi})$.

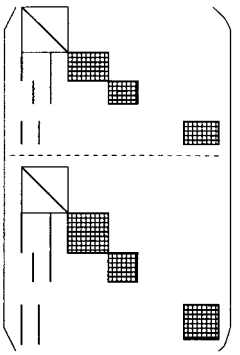

Figure 4. Form of the projection operator Q.

the nodes, the operator Q has a block structure shown in Figure 4. The matrix Q consists of two submatrices of similar structure stacked on top of each other. This decomposition arises from the fact that the mortars always have two sides to connect. Diagonal blocks at the left top of each of the two submatrices impose conditions on the vertices for the two sides of the mortar. Each gridded box corresponds to a transformation between an individual mortar and its side and consists of the coefficients Q_{qm} defined in Equation (48). For each of the gridded blocks in Q there are two columns to the left. These columns correspond to the terms T_{ql}, $l = 0, \bar{N}$ in Equation (48).

Note that in the case when the grid is conforming everywhere, the projection operator (47) becomes an identity operator and Q is simply a stack of two unity operators

$$Q = \begin{pmatrix} I \\ I \end{pmatrix} \tag{50}$$

3.4. Discrete equations

Let u^p be the vector of unknowns that correspond to the nodal points in a conforming subregion Ω_p, including those nodal points that lie on the skeleton S. Let r^p be the vectors of the corresponding right-hand side values, and A^p is the linear operator that is a discrete analog of Equation (23) in Ω_p, with appropriate boundary conditions on physical boundaries and weak Neumann boundary conditions on S.

We then construct a global vector u such that it contains all the nodal values in all the subdomains Ω_p, $p = 1, \ldots, P$, and the nodes that lie on S are ordered first: $u = (u^S, u^I)^T$. The right-hand side vector $r = (r^S, r^I)^T$ is constructed accordingly. A global operator A is then obtained by regrouping rows of a block diagonal matrix

$$\begin{pmatrix} A^1 & & & \\ & \ddots & & \\ & & A^p & \\ & & & \ddots \end{pmatrix} \tag{51}$$

to yield a system of linear equations

$$\begin{pmatrix} A_{SS} & A_{SI} \\ A_{IS} & A_{II} \end{pmatrix} \begin{pmatrix} u^S \\ u^I \end{pmatrix} = \begin{pmatrix} r^S \\ r^I \end{pmatrix} \tag{52}$$

The solution of linear system (52) has a discontinuity at the nonconforming interface S. Following Reference [10], in order to minimize the error, we solve the following problem:

$$\begin{pmatrix} Q^T & \\ & I \end{pmatrix} \begin{pmatrix} A_{SS} & A_{SI} \\ A_{IS} & A_{II} \end{pmatrix} \begin{pmatrix} Q & \\ & I \end{pmatrix} \begin{pmatrix} \phi \\ u^I \end{pmatrix} = \begin{pmatrix} Q^T & \\ & I \end{pmatrix} \begin{pmatrix} r^S \\ r^I \end{pmatrix} \tag{53}$$

It is easy to see that a solution of Equation (53) satisfies simultaneously two sets of requirements. First, it solves all the systems $A^p u^p = r^p$ corresponding to each of the subregions Ω_p. Second, the nodal values u^S, which belong to S, are obtained by projection (49), where the vector ϕ satisfies a problem

$$Q^T(A_{SS}Q\phi + A_{SI}u^{\mathrm{I}} - r^S) = 0 \tag{54}$$

Note that when a grid is conforming, the projection operator Q becomes stack of two unit matrices (50); and problem (54) results in the standard summation of elemental stiffness matrices for those elements that share the interface.

If the problem is integrated explicitly in time, matrices A^p become diagonal mass matrices, the computation of internal nodal values u^{I} decouples from the computation of interfacial values u^S. The former are obtained by an identical procedure to that used in the conforming formulation. The latter are projected from the mortar nodal values ϕ, which are the solutions of a problem

$$Q^T M_{SS} Q\phi = Q^T r^S$$

where M_{SS} is a diagonal mass matrix for the interfacial nodes. It is relatively easy to invert the operator $Q^T M_{SS} Q$, because the values belonging to different mortars $\gamma_i \in S$ are coupled loosely. Using Gaussian elimination, it is possible to decouple the computation of the mortar vertices from the rest. After that, each mortar block can be computed independently.

If the problem is solved implicitly, then problem (53) can be solved iteratively. A variety of domain decomposition preconditioners can be applied to improve the convergence of an iterative solver [18–21].

4. A THREE-DIMENSIONAL NONCONFORMING SPECTRAL ELEMENT MODEL

In geophysical applications, we usually deal with grids that have a complicated horizontal structure, but are fairly simple in the vertical. For these grids, the nonconforming two-dimensional formulation of Section 3 can be easily modified to apply in three dimensions.

In the spectral element model of Iskandarani *et al.* (submitted), the number of elements in the vertical is always the same, and vertical element edges are always parallel to z (see Figure 5 for a sample spectral element grid in the vertical). In this case, coordinate transformation between a physical space (x, y, z) and a computational space (ξ, η, σ) has the form

$$x = x(\xi, \eta), \qquad y = y(\xi, \eta), \qquad z = z(\xi, \eta, \sigma) \tag{55}$$

Since the vertical structure is simple, it is not necessary to use a nonconforming grid in the vertical. The difference between the formulation above and the one that follows is in using tensor product polynomial spaces in definitions of mortar and projection spaces in both Equations (27) and (31). The spaces are defined over a two-dimensional nonconforming mortar face instead of a one-dimensional mortar line.

The basis functions for the two spaces are a tensor product of two-dimensional basis functions, as defined in Section 3.2 and the standard Legendre cardinal functions in the vertical. Consider a mortar interface. Let N denote the order of spectral expansion for an element edge, let $\bar{N}$ be the order for a mortar and N^σ denote the order of spectral interpolation in the vertical. Then, along a two-dimensional mortar face, any variable u and any mortar function ϕ are interpolated respectively as

$$u(x(\xi), y(\xi), z(\xi, \sigma)) = \sum_{i=0}^{N} \sum_{k=0}^{N^\sigma} u_i^k h_i^N(\xi) h_k^{N^\sigma}(\sigma)$$

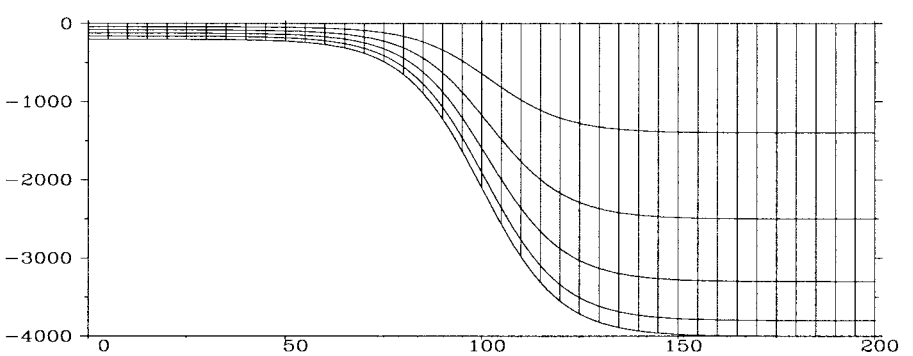

Figure 5. Vertical slice of a sample three-dimensional SEOM grid showing the elemental partition. The elements are refined near the bottom to resolve the gradients of a density front traveling down an idealized shelf break. The vertical scale is in meters and the horizontal scale is in kilometers.

$$\phi(\bar{x}(\bar{\xi}), \bar{y}(\bar{\xi}), \bar{z}(\bar{\xi}, \sigma)) = \sum_{m=0}^{\bar{N}} \sum_{k=0}^{N^\sigma} \phi_m^k h_m^{\bar{N}}(\bar{\xi}) h_k^{N^\sigma}(\sigma) \tag{56}$$

The basis functions for the projection space $\tilde{P}$ is a tensor product

$$\psi_i^N(\xi) h_k^{N^\sigma}(\sigma) \tag{57}$$

where ψ_i^N is defined in Equations (38)–(40).

The projection operator between a mortar and its side is obtained by substituting formulas (56) and (57) into the integral in (30). Using Gauss–Lobatto quadratures of order N and $\bar{N}$ where appropriate for the horizontal integration, and of order N^σ for the vertical integration, we decouple the projection operator into separate projection operators for each vertical level. For each vertical level r the integration gives

$$B_q^r u_q^r = \sum_{m=0}^{\bar{N}} P_{qm}^r \phi_m^r - R_{q0}^r \phi_0^r - R_{q\bar{N}}^r \phi_{\bar{N}}^r, \quad q = 1, \ldots, R \tag{58}$$

where B_q^r is assembled from the elemental contributions of the form

$$B_q^r = \omega_q^N \omega_r^{N^\sigma} |s_q^{\Gamma_j}| z_\sigma(\xi_i^N, \sigma_r^{N^\sigma}) \tag{59}$$

Similarly, the terms P_{qm}^r, R_{q0}^r and $R_{q\bar{N}}^r$ are obtained from elemental contributions of the form

$$P_{qm}^r = \sum_{s=0}^{\bar{N}} h_m^{\bar{N}}(\bar{\xi}(\xi_s^{\bar{N}})) \psi_q(\xi_s^{\bar{N}}) \omega_s^{\bar{N}} \omega_r^{N^\sigma} |S_s^{\Gamma_j}| z_\sigma(\xi_s^{\bar{N}}, \sigma_r^{N^\sigma})$$

$$R_{q0}^r = \psi_q(-1) \omega_0^N \omega_r^{N^\sigma} |s_0^{\Gamma_j}| z_\sigma(-1, \sigma_r^{N^\sigma})$$

$$R_{q\bar{N}}^r = \psi_q(1) \omega_N^N \omega_r^{N^\sigma} |s_N^{\Gamma_j}| z_\sigma(1, \sigma_r^{N^\sigma}) \tag{60}$$

The elemental assembly is done in both the horizontal and the vertical, the metric term $|s_i^{\Gamma_j}| z_\sigma(\xi_i^N, \sigma_r^{N^\sigma})$ is obtained by computing the Jacobian of the coordinate transformation $x(\xi), y(\xi), z(\xi, \sigma)$. Construction of the global projection operator for each vertical level then proceeds in exactly the same way as it is done in Sections 3.3 and 3.4.

The two-dimensional projection operators are used for each prognostic variable in Equation (23) and three-dimensional projection operators are used for all prognostic variables in Equations (20) and (21). Combining Equations (20), (21) and (23) on each conforming subregion with projection operators on the interface for all two-dimensional and three-dimensional prognostic variables, we arrive at problem (53), where ϕ are the values of all prognostic variables on the interface, and u_I are the values of all prognostic variables in the interior of the conforming regions.

We integrate the problem split explicitly in time, wherein several shorter time steps are taken to advance the two-dimensional variables before a single time step for the three-dimensional variables is taken. Problem (53) is constructed and solved for each variable independently

every time step, and the computation of the interfacial and internal values are decoupled from each other.

5. CONVERGENCE TESTS

5.1. Convergence tests in two dimensions

The two-dimensional formulation is tested on two simple problems. One is the diffusion equation in a unit square, $\Omega = [0, 1][0, 1]$

$$\frac{\partial u}{\partial t} - \nu \nabla^2 u = 0 \quad \text{on } \Omega \tag{61}$$

subject to initial and boundary conditions of the form

$$u(x, y, 0) = \cos(\pi x)\sin(\pi y) + 0.25\cos(6\pi x)\sin(6\pi y)$$

$$u(x, 0, t) = u(x, 1, t) = 0, \qquad u_x(0, y, t) = u_x(1, y, t) = 0$$

where $\nabla^2 = (\partial^2/\partial x^2) + (\partial^2/\partial y^2)$ is a two-dimensional Laplacian operator and $\nu = 0.1$.

The second problem is a two-dimensional linear shallow water equation

$$\frac{\partial \vec{u}}{\partial t} + \nabla h = 0$$

$$\frac{\partial h}{\partial t} + \nabla \cdot (\vec{u}) = 0 \tag{62}$$

where $\vec{u} = (u, v)$ is a two-dimensional velocity vector, h is a surface elevation, $\nabla = (\partial/\partial x, \partial/\partial y)$ is a gradient operator. This problem is solved in a unit square Ω with free slip boundary conditions $\vec{u} \cdot \vec{n}$ on $\partial\Omega$, and is initialized with

$$\vec{u} = 0$$

$$h = \cos(\pi x)\cos(\pi y) + 0.25\cos(6\pi x)\cos(\pi y)$$

Both problems have an analytic solution, which is

$$u = \mathrm{e}^{-2\pi^2 \nu t}\cos(\pi x)\sin(\pi y) + 0.25\,\mathrm{e}^{-72\pi^2 \nu t}\cos(6\pi x)\sin(6\pi y)$$

for problem (61) and

$$u = \frac{1}{\sqrt{2}} \{\sin(\sqrt{2}\pi t)\sin(\pi x)\cos(\pi y) + 0.25\sin(6\sqrt{2}\pi t)\sin(6\pi x)\cos(6\pi y)\}$$

$$v = \frac{1}{\sqrt{2}} \{\sin(\sqrt{2}\pi t)\cos(\pi x)\sin(\pi y) + 0.25\sin(6\sqrt{2}\pi t)\cos(6\pi x)\sin(6\pi y)\}$$

$$h = \cos(\sqrt{2}\pi t)\cos(\pi x)\cos(\pi y) + 0.25\cos(6\sqrt{2}\pi t)\cos(6\pi x)\cos(6\pi y)$$

for problem (62).

The problems are solved on five different nonconforming grids to study convergence to their analytic solutions. The coarsest grid is shown in Figure 6. Each of the elements on the right part of the grid matches two elements on the left through a mortar interface. Spectral expansion in the right portion of the grid is 9, and in the left portion of the grid it is 5. The other grids are obtained by using more elements with the same spectral expansions of 9 and 5 in the right and left parts of the grid respectively. The resulting convergence curve is compared with convergence results on two sets of conforming grids. One set has a spectral expansion of 9 and larger elements, similar to those on the right part of the grid in Figure 6. The second set of conforming grids has a spectral expansion of 5 and smaller elements. Figure 7(a) shows the log–log plot of maximum error versus the number of unknowns for the diffusion problem on the nonconforming and two different conforming sets of grids. Figure 7(b) shows similar information for the shallow water problem. Here we give the error for the u velocity only; the two other variables have similar convergence properties. The time step is 10^{-5} for the diffusion problem and 10^{-3} for the shallow water problem, it is chosen small enough to make the time discretization error negligible compared with that of the space discretization.

The refinement that we use is of a h-type and it results in an algebraic convergence. In both problems, the convergence of the nonconforming simulation is almost identical to that for the lower-order conforming simulation. The shallow water problem exhibits a much slower convergence rate than for the diffusion problem on both the conforming and nonconforming grid. However, accuracy in both problems is not degraded on a nonconforming grid.

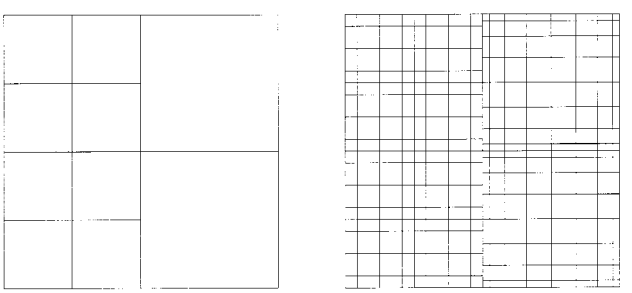

Figure 6. The nonconforming grid for the diffusion and linear shallow water problems. The grid consists of two conforming regions. The left panel shows element edges. The right panel shows the full mesh.

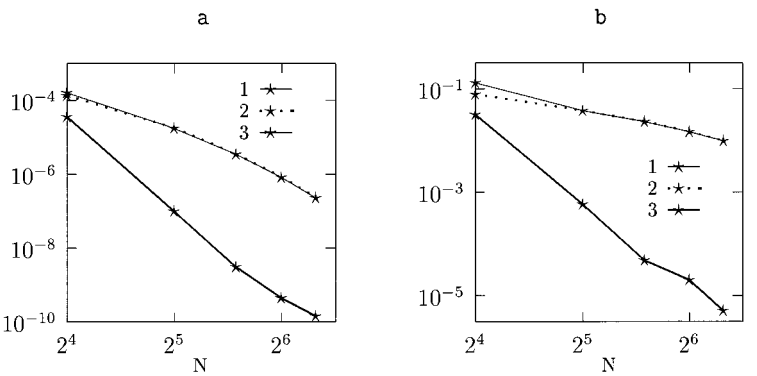

Figure 7. Convergence to the analytic solution for (a) the two-dimensional diffusion problem and (b) the shallow water problem. N, number of grid points in each direction; 1, nonconforming grid; 2, conforming with a spectral expansion of 5; 3, conforming with a spectral expansion of 9.

5.2. Convergence tests in three dimensions

To test an extension of a nonconforming formulation to the three-dimensional case, we solve a diffusion equation

$$\frac{\partial u}{\partial t} - \nu \nabla^2 u = 0 \quad \text{on } \Omega \tag{63}$$

in a unit cube $\Omega = [0, 1][0, 1][0, 1]$, where

$$\nabla^2 = \frac{\partial^2}{\partial x^2} + \frac{\partial^2}{\partial y^2} + \frac{\partial^2}{\partial z^2}$$

is a three-dimensional Laplacian operator. Initial and boundary conditions are

$$u(x, y, z, 0) = \cos(\pi z)\{\cos(\pi x)\cos(\pi y) + 0.25\cos(6\pi x)\cos(6\pi y)\}$$

$$\nabla u \cdot n = 0 \quad \text{on } \partial\Omega$$

We study convergence to the analytic solution of the form

$$u = \cos(\pi z)\{e^{-3\pi^2 \nu t}\cos(\pi x)\cos(\pi y) + 0.25\, e^{-73\pi^2 \nu t}\cos(6\pi x)\cos(6\pi y)\}$$

using the same refinement strategy and time step as in Section 5.1. As before, we create three sets of grids: one nonconforming and two conforming. In the horizontal, the grids are similar to the ones described in Section 5.1. In the vertical, all the grids are conforming; they have a spectral expansion of 9 and the number of elements is such that the resolution in z matches

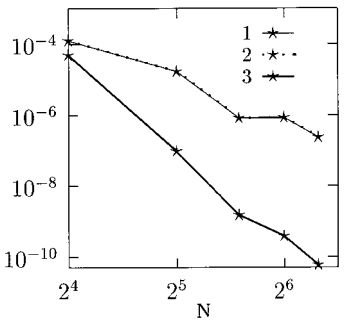

Figure 8. Convergence to the analytic solution for the three-dimensional diffusion problem. N, number of grid points in each direction. 1, nonconforming grid; 2, conforming with a spectral expansion of 5; 3, conforming with a spectral expansion of 9.

that of x and y. Figure 8 shows a log–log plot of the maximum error in solving the diffusion problem for the three sets of experiments. As in the two-dimensional diffusion problem, the nonconforming problem exhibits the same convergence rate as the conforming problem with lower spectral expansion.

The second three-dimensional test problem is Baroclinic Kelvin Waves (BKW) in a periodic channel. BKW are internal gravity waves modified by rotation [22,23]. The BKW solution can be obtained by expanding variables in the linearized primitive equations

$$u_t - fv = \frac{-P_x}{\rho_0} - g\zeta_x$$

$$v_t + fu = \frac{-P_y}{\rho_0} - g\zeta_y$$

$$P_z = -\rho' g$$

$$u_x + v_y + w_z = 0$$

$$\rho'_t + w\bar{\rho}_z = 0 \tag{64}$$

in the series of $e^{i(kx-\sigma t)}$, where x is the periodic direction. In Equations (64), (u, v, w) are components of a three-diemensional velocity vector, ρ is the density, such that

$$\rho = \rho_0 + \bar{\rho}(z) + \rho'(x, y, z, t)$$

P is the perturbation pressure, f is the Coriolis parameter, g is the gravitational constant, ζ is the free surface displacement.

The periodic channel is of depth H and the free-slip boundary conditions at the channel boundaries $y = 0$, $y = L$. Let the positive direction of z be upward, with $z = 0$ at the surface. In this vertical coordinate, the boundary conditions are

$$\zeta_t = w \quad \text{on } z = 0$$
$$w = 0 \quad \text{on } z = -H$$
$$P = 0 \quad \text{on } z = 0$$

Equations (64) have an analytic solution, which in the case when $\bar{\rho}(z)$ is constant, has the form

$$u = A_u \cos \beta(z + H) F_{\cos}(x, y, t)$$

$$v = 0$$

$$w = A_w \sin \beta(z + H) F_{\sin}(x, y, t)$$

$$\zeta = A_\zeta F_{\cos}(x, y, t)$$

$$\frac{\rho'}{\rho_0} = A_\rho \sin \beta(z + H) F_{\cos}(x, y, t)$$

$$\frac{P}{\rho_0} = A_P \{\cos \beta(z + H) - \cos \beta H\} F_{\cos}(x, y, t)$$

where β is obtained from the relation $\beta \tan \beta H = N^2/g$, the Brunt–Vaisala frequency is defined as $N^2 = -g\bar{\rho}_z/\rho_0$, functions $F_{\cos}$ and $F_{\sin}$ are given by

$$F_{\cos} = \mathrm{e}^{-\mu y} \cos(kx - \sigma t), \qquad F_{\sin} = \mathrm{e}^{-\mu y} \sin(kx - \sigma t)$$

and $A_u = k/\sigma$, $A_w = k/N$, $A_\zeta = \cos \beta H/g$, $A_\rho = \beta/g$, $A_P = 1$, where $\sigma = kN/\beta$, $\mu = \beta f/N$. We consider the propagation of the superposition of two modes: $k = 1$ and $k = 6$. As before, we solve the problem on the grids of five different resolutions. The horizontal structure of the coarsest of the nonconforming grids in shown schematically in Figure 9. One part of the channel has the grid with spectral expansion of 5, and the rest use the spectral expansion of 9. Refinement is done, as before, by splitting to larger number of elements. For comparison, we also show convergence for the two sets of conforming grids, one has the spectral expansion of 9 everywhere, and the other has a spectral expansion of 5. In the vertical, all the grids have the same structure: they have four elements with spectral expansion of 9 in each. With $H = 1000$ m, and $L = 200$ km, the error due to the vertical discretization is negligible compared with the error due to the horizontal dicsretization. The time step is 1.

Figure 10(a)–(c) shows the maximum error in u, v and ζ respectively for the three sets of experiments. The curves have a similar rate of convergence. The errors in the nonconforming simulation are close to the ones obtained on the conforming grids with lower spectral expansion.

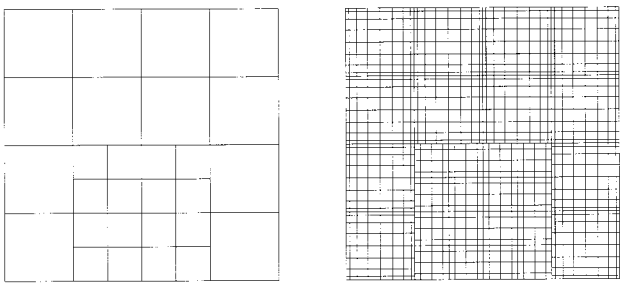

Figure 9. The nonconforming grid for the BKW problem. The left panel shows element edges. The right panel shows the full mesh.

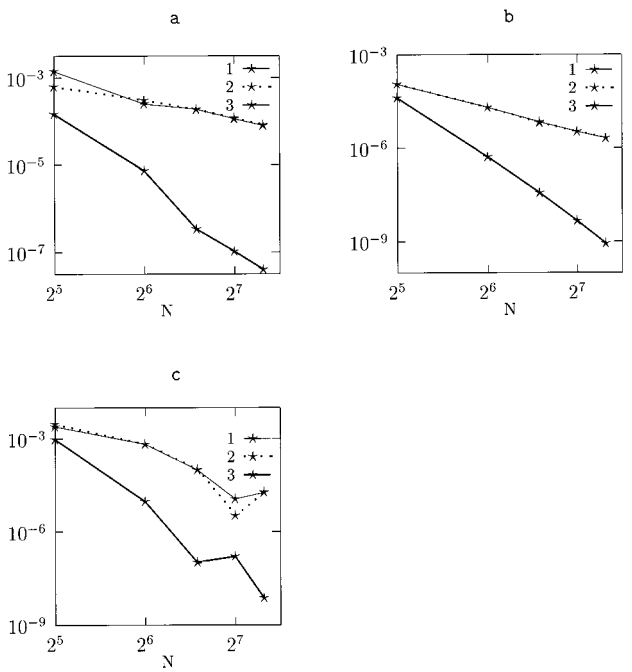

Figure 10. Convergence to the analytic solution for the BKW problem. (a) Maximum u velocity error, (b) maximum v velocity error, (c) maximum error in free surface ζ. N, number of grid points in each direction; 1, nonconforming grid; 2, conforming with a spectral expansion of 5; 3, conforming with a spectral expansion of 9.

6. SIMULATIONS IN THE NORTHWEST ATLANTIC

In this section we show results of two nonconforming, reduced-gravity shallow water simulations in a 'realistic' domain. The reduced-gravity shallow water problem is a modification of a classic shallow water problem, obtained in a two-layer fluid, where one layer consists of an infinite depth motionless fluid of density ρ_1 and the other layer is an active layer of density ρ_2 (see Reference [24]). The resulting equations differ from the classic shallow water equations only in a definition of a gravitational constant and a fluid depth. The gravitational constant is now scaled by the ratio of the two different densities, $(\Delta\rho/\rho_1)g$, and the fluid depth is the depth of the active layer. Compared with the classic shallow water model, the major length scales in the reduced-gravity shallow water model are closer to that of the stratified model [24].

First, we investigate propagation of a Kelvin wave in a closed basin of irregular structure. The basin is between 25° and 45°N and 50° and 76°W, which covers a large portion of the Northwest Atlantic. The grid is shown in Figure 11. It is nonconforming and consists of two conforming subregions. One subregion covers the Gulf of Maine and a part of the North Atlantic Ocean adjacent to it. It has a relatively low spectral expansion (5 for velocity nodes and 3 for pressure). The second subregion covers the rest of the domain. It is constructed of larger elements with higher spectral expansions (7 for velocity and 5 for pressure). Both subregions have an average resolution of 10 km. In the simulation, the gravitational constant is set to $g = 0.05\ \mathrm{m\,s^{-2}}$ and the depth of active layer is 600 m. The time step is 120 s.

We are interested here in a behavior of the wave as it passes through a nonconforming interface. The wave is initialized at the outer boundary of the domain, as shown in Figure 12(a). The initial perturbation of a free surface displacement ζ has the form

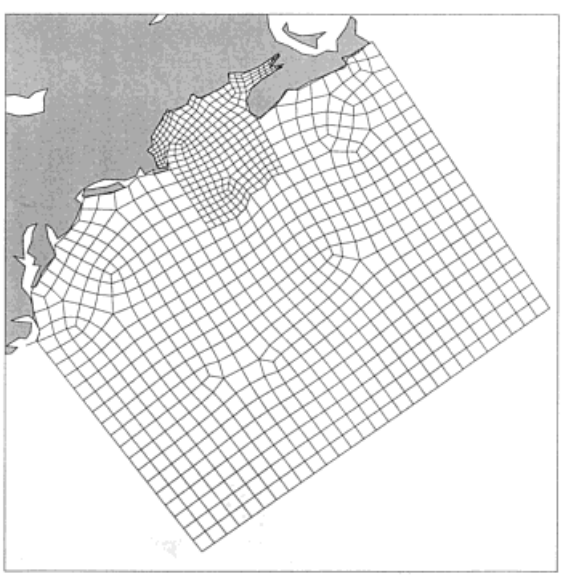

Figure 11. Nonconforming grid in the North Atlantic. Only element edges are shown.

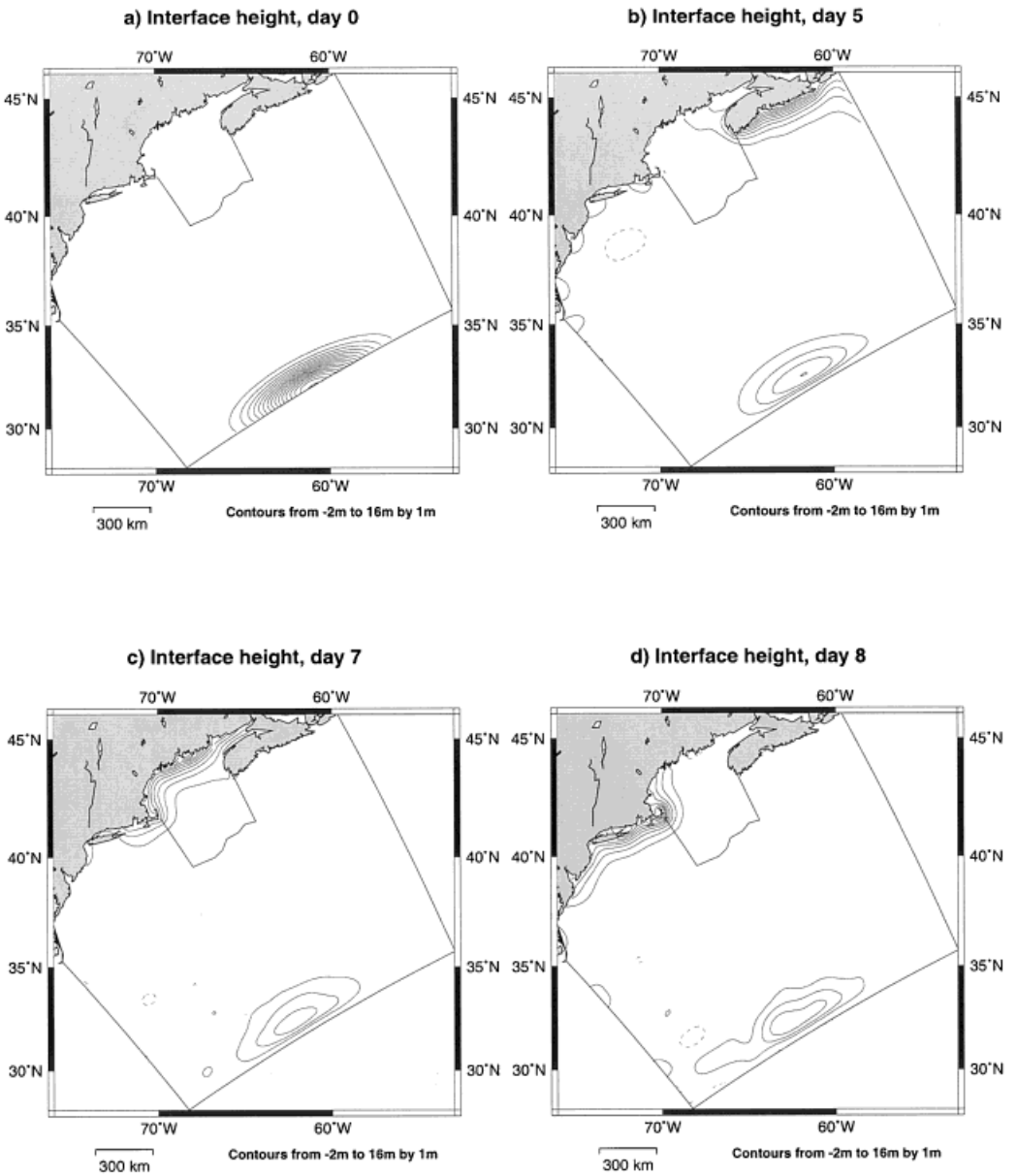

Figure 12. Contour plots of the interface height in the Kelvin wave experiment. (a) Initial conditions, (b)–(d) plots at day 5, 7, 8 respectively. Positive contours are given with solid lines, negative ones with dashed lines. The interface between grids is outlined.

$$\zeta = A \exp\left(\frac{x^2}{L_x} + \frac{y^2}{L_y}\right)$$

where x, y are the coordinates in a rotated coordinate system, such that the x-direction is aligned with the outer boundary, and the origin is at the center of it. Parameters $L_x = 300$ km and $L_y = 100$ km are length scales of the perturbation along and across the boundary respectively, and $A = 16$ m. The initial velocity is set to zero. In the simulation, a harmonic viscosity of 100 $m^2\,s^{-1}$ is used. The Coriolis force is set to the standard $2\Omega \sin \lambda$, where Ω is the Earth rotation rate, and λ is a latitude.

Within the next several days, the perturbation travels counterclockwise along the boundary. A weak residual signal remains in the position of the initial condition, its westward propagation is rather slow compared with the propagation of the Kelvin wave. The residual signal is a result of an initial geostrophic adjustment, as described in Reference [22]. At around day 5, the counterclockwise perturbation enters the coast of the Gulf of Maine. Figure 12(b) shows how it passes the interface between the two nonconforming grids on the way into the Gulf of Maine, and Figure 12(c) and (d) shows the wave propagating along the Gulf of Maine coast and then coming out of the Gulf through a nonconforming interface. The figures clearly demonstrate that the shape of the wave is unaffected by the interface. For comparison we performed a similar simulation on a conforming grid. The r.m.s. difference in surface elevation between the two simulations at day 8 is about 1 per cent of the signal.

The second problem is a monopole vortex solution. The vortex evolves in a nonlinear way as described in References [22,25]. The problem is solved on a same grid as the previous problem. It is a reduced-gravity simulation with the same g and h as before. The initial conditions are the Gaussian profile for the free surface $\zeta = A \exp[((x - x_c)^2 + (y - y_c)^2)/L^2]$. The length scale is $L = 50$ km, which is approximately half of the Rossby deformation radius for the mid-latitude ocean. The vortex is positioned one L-scale to the east of the interface, as shown in Figure 13(a). The initial velocity field is in a steady f-plane gradient wind balance [24] with the initial surface elevation. The simulation uses harmonic viscosity of 150 $m^2\,s^{-1}$ and a time step of 120 s.

Westward propagation of the vortex and its interaction with the interface is shown in Figure 13(b)–(d). Its center passes close to the corner in the interface and the vertex emerges on the other side of the interface 'unharmed'. East of the vertex, a negative lobe is formed in a wake of a Rossby wave. The lobe passes through the interface as well.

7. CONCLUSION

A nonconforming SEOM model based on the SEOM of Iskandarani *et al.* [3]; Iskandarani *et al.* (submitted)] and mortar element method of Maday *et al.* [10] is proposed and tested on a series of problems in two and three dimensions. The method is designed for problems wherein different flow regimes and/or different geometric requirements are present within a single simulation. For such problems, the combination of high- and low-order methods helps to get good accuracy in regions with smooth properties, and localize the errors near the fronts and sharp geometric and topographic features. The method also allows local mesh refinement, which simplifies grid generation for a problem in a complicated domain.

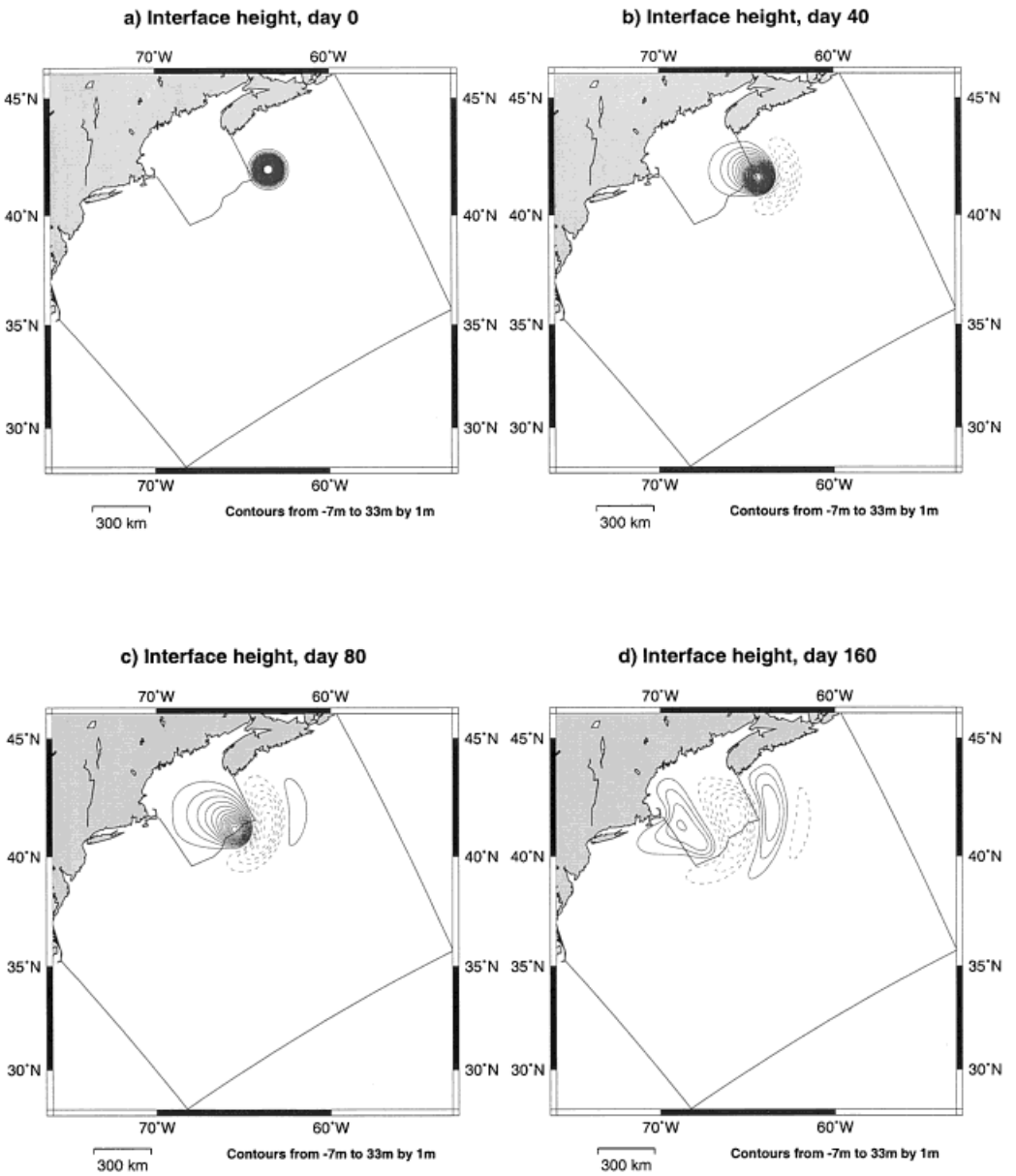

Figure 13. Contour plots of the interface height in the monopole vortex experiment. (a) Initial conditions, (b)–(d) plots at day 40, 80, 160 respectively. Positive contours are given with solid lines, negative ones with dashed lines. The interface between grids is outlined.

Several test problems that have an analytic solution have been used to verify an analytic convergence rate obtained by Bernardi *et al*. [13] for nonconforming elliptic problems. The results show that convergence rates are similar in the conforming and nonconforming simulations. The method has also given good convergence properties for a number of hyperbolic problems, such as a linear shallow water problem and a three-dimensional Kelvin wave problem. The method has been also applied in a reduced-gravity form to a problem in a realistic geometry. Propagation of Kelvin waves and a monopole vortex problem have been simulated on a nonconforming grid in the Northwest Atlantic. The simulations have shown that the waves pass the interface without generating any distortions to their shape and wave speed.

The mortar element method described in Section 3 is applied here to the spectral element model. Simply by changing the order of the basis functions on the interface, it is possible to construct a combined spectral–finite element model, based on the same formulation of the nonconforming interface. The mortar element formalism can also be used to couple together different Galerkin spectral and finite element ocean models, if they solve the same set of equations, use the same time stepping and have similar treatment of fluxes.

ACKNOWLEDGMENTS

The authors would like to thank Daniel R. Lynch for his helpful comments. Development and application of the nonconforming SEOM is supported by grants from the NSF Division of Ocean Sciences (OCE9632809) and the Office of Naval Research (N000149310197).

REFERENCES

1. Curchitser EN, Iskandarani M, Haidvogel DB. A spectral element solution of the shallow water equations on multiprocessor computers. *Journal of Atmospheric and Oceanographic Technology* 1998; **15**(2): 510–521.
2. Haidvogel DB, Curchitser E, Iskandarani M, Hughes R, Taylor M. Global modeling of the ocean and atmosphere using the spectral element method. *Atmosphere–Ocean* 1997; **35**: 505–531.
3. Iskandarani M, Haidvogel DB, Boyd JP. A staggered spectral element model with application to the oceanic shallow water equations. *International Journal for Numerical Methods in Fluids* 1995; **20**: 393–414.
4. Levin JG, Iskandarani M, Haidvogel DB. A spectral filtering procedure for eddy-resolving simulations with a spectral element ocean model. *Journal of Computational Physics* 1997; **137**(1): 130–154.
5. Wingate B, Boyd JP. Spectral element methods on triangles for geophysical fluid dynamic problems. In *Proceedings of the Third International Conference On Spectral and High-Order Methods*. Ilin AV, Scott LR (eds). Houston, TX, Houston Journal of Mathematics: Texas, 1996; 305–317.
6. Taylor M, Tribbia J, Iskandarani M. The spectral element method for the shallow water equations on the sphere. *Journal of Computational Physics* 1997; **130**(1): 92–108.
7. Wunsch C, Haidvogel DB, Iskandarani M, Hughes R. Dynamics of the long-period tides. *Progress in Oceanography* 1997; **40**: 81–108.
8. Funaro D, Quateroni A, Zanolli P. An interative procedure with interface relaxation for domain decomposition methods. *SIAM Journal for Numerical Analysis* 1988; **25**: 1213–1236.
9. Bernardi C, Madai Y, Sacchi Landriani G. Nonconforming matching conditions for coupling spectral and finite element methods. *Applied Numerical Mathematics* 1990; **6**: 65–84.
10. Maday Y, Mavriplis C, Patera AT. Nonconforming mortar element method: application to spectral discretizations. In *Domain Decomposition Methods*, Chan T, Periaux J, Widlund O (eds). SIAM: Philadelphia, PA, 1989; 392–418.
11. Anagnostou G, Maday Y, Mavriplis C, Patera AT. On the mortar element method: generalization and implementation. In *Third International Conference on Domain Decomposition Methods for Partial Differential Equations*, Glowinski R (ed.). SIAM: Philadelphia, PA, 1990; 157–173.

12. Bernardi C, Debit N, Madai Y. Coupling finite element and spectral methods: first results. *Mathematics of Computation* 1990; **54**(189): 21–39.
13. Bernardi C, Maday Y, Patera AT. A new nonconforming approach to domain decomposition: the mortar element method. In *Non-linear Partial Differential Equations and their Applications*, vol. 11, Brezis H, Lions JL (eds). Pitman/Wiley: London/New York, 1994; 13–51.
14. Haidvogel DB, Beckmann A. *Numerical Ocean Circulation Modeling*. Imperial College Press: London, 1999.
15. Maday Y, Patera AT. Spectral element methods for the incompressible Navier–Stokes equations. In *State of the Art Surveys in Computational Mechanics*, Noor AK (ed.). ASME: New York, 1988; 71–143.
16. Patera AT. A spectral element method for fluid dynamics: laminar flow in a channel expansion. *Journal of Computational Physics* 1984; **54**: 468–488.
17. Boyd JP. *Chebyshev and Fourier Spectral Methods*. Springer: Berlin, 1989.
18. Bjorstad PE, Widlund OB. Iterative methods for the solution of elliptic problems on regions partitioned into substructures. *SIAM Journal of Numerical Analysis* 1986; **23**: 1097–1120.
19. Bramble JH, Pasciak JE, Schatz AH. The construction of preconditioners for elliptic problems by substructuring. I. *Mathematics of Computation* 1986; **47**: 103–134.
20. Dryja M. A capacitance matrix method for Dirichlet problems on polygonal regions. *Numerische Mathematik* 1982; **39**: 51–64.
21. Golub GH, Mayers D. The use of pre-conditioning over irregular regions. In *Computing Methods in Applied Sciences and Engineering*, *VI*, Glowinski R, Lions J-L (eds). Elsevier: Amsterdam, 1984; 3–14.
22. Miliff RF, McWilliams JC. The evolution of boundary pressure in ocean basins. *Journal of Physical Oceanography* 1994; **24**(6): 1317–1338.
23. Hendershott MC. Long waves and ocean tides. In *Evolution of Physical Oceanography*, Warren BA, Wunsch C (eds). MIT Press: Boston, MA, 1981; 292–371.
24. Cushman-Roisin B. *Introduction to Geophysical Fluid Dynamics*. Prentice-Hall: Englewood Cliffs, NJ, 1994.
25. McWilliams JC, Flierl GR. On the evolution of isolated non-linear vortices. *Journal of Physical Oceanography* 1979; **9**: 1155–1182.

